POLITECNICO DI TORINO
Repository ISTITUZIONALE

Factor screening for adaptive powder feeding in Laser-Beam Directed Energy Deposition

Original
Factor screening for adaptive powder feeding in Laser-Beam Directed Energy Deposition / Pilagatti, A.N., Vini, J., Atzeni, E., Salmi, A., Manfredi, D.. - In: INTERNATIONAL JOURNAL, ADVANCED MANUFACTURING TECHNOLOGY. - ISSN 0268-3768. - (2026). [10.1007/s00170-026-17941-w]

Availability:
This version is available at: 11583/3012329 since: 2026-06-22T08:35:45Z

Publisher:
Springer

Published
DOI:10.1007/s00170-026-17941-w

Terms of use:

This article is made available under terms and conditions as specified in the corresponding bibliographic description in the repository

Publisher copyright

(Article begins on next page)

18 November 2026

The International Journal of Advanced Manufacturing Technology
https://doi.org/10.1007/s00170-026-17941-w

ORIGINAL ARTICLE

Factor screening for adaptive powder feeding in Laser-Beam Directed Energy Deposition

Adriano Nicola Pilagatti[1] · Josip Vinčić[2,3] · Eleonora Atzeni[1] · Alessandro Salmi[1] · Diego Manfredi[4]

Received: 31 October 2025 / Accepted: 18 March 2026
© The Author(s) 2026

Abstract
Laser beam powder directed energy deposition (DED-LB/Powder) is a promising additive manufacturing (AM) technology for large parts, repairs, and multi-material builds, yet many process parameters govern part quality. This study investigates how these parameters affect powder delivery and deposition height for AISI 316L. A moving control-volume model is coupled with a factor-screening design to relate powder feed settings to travel speed and to assess four responses: height, density, porosity, and microhardness. Within the tested window, final height is primarily governed by the Z-increment (ΔZ), with additional contributions from energy density (E), overlap efficiency (O_e), and κ. The approach is evaluated through a design of experiments that demonstrates sensitivity to selected factors and their impact on specimen responses. Boundary conditions in the building chamber are monitored with a custom system. A full-factorial plan with replication, randomization, and blocking is used, and analysis of covariance (ANCOVA) identifies which factors and noise sources affect each response. The results map factor effects and interactions, provide simple response surfaces for height control without real-time feedback, and indicate that density and hardness are relatively insensitive within the tested ranges, whereas porosity requires dedicated analysis. The study also highlights non-significant factors that can be deprioritized in subsequent optimization and robustness studies.

Keywords Additive manufacturing · Process parameters · Design of experiment · Directed energy deposition · AISI 316L

1 Introduction

Directed energy deposition (DED) is a category of additive manufacturing (AM) processes that utilizes a focused thermal energy to melt feedstock material on a substrate and build up a part along a programmed deposition path. The thermal sources used in DED are either a laser beam (LB), an electric arc (Arc), or an electron beam (EB). The feedstock material can be supplied either as a continuous wire or as a powder stream. The DED process that employs an LB as the thermal source for fusing powdered material is referred to as DED-LB/Powder, as per ISO/ASTM 52900:2021(E) [1]. This process is highly efficient and capable of producing large parts. It has great potential for repair operations as it can deposit material on existing parts [2, 3]. A high-quality DED part refers to a component that exhibits desired characteristics in terms of dimensions, morphology, and microstructure, thereby ensuring its suitability for the intended application [4].

✉ Adriano Nicola Pilagatti
adriano.pilagatti@polito.it

1 Department of Management and Production Engineering (DIGEP), Politecnico di Torino, Corso Duca degli Abruzzi 24, Torino 10129, Italy

2 Chair of Materials Engineering of Additive Manufacturing, TUM School of Engineering and Design, Technical University of Munich, Freisinger Landstraße 52, Garching bei München 85748, Germany

3 Munich Institute of Integrated Materials, Energy and Process Engineering (MEP), Technical University of Munich, Lichtenbergstraße 4a, Garching bei München 85748, Germany

4 Department of Applied Science and Technology (DISAT), Politecnico di Torino, Corso Duca Degli Abruzzi, 24, Torino 10129, Italy

Published online: 23 May 2026

A critical challenge in DED processes is ensuring controlled growth during deposition. In DED-LB/Powder, the layer thickness is directly influenced by process parameters and deposition dynamics. Maintaining a constant distance between the deposition head and the substrate during deposition is crucial, as this involves maintaining the laser and powder focus on the top surface of the substrate [5]. Moreover, in DED, there may be cases where different deposited heights are desired within the same section (layer), for example, in the fabrication of curved structures, where non-parallel slicing is applied. The ability to control deposition height variation within the same component is crucial for process adaptability and optimization. In parallel, it is of great importance to know the actual deposited height during deposition of the part. Given the practical implications of this problem, several works in the literature have explored the possibility of controlling the deposition height and minimize deviations. Monitoring approaches have been proposed, based on the acquisition of melt pool temperature and the adjustment of process parameters. Among these, the laser power is typically adopted as a control parameter, due to its shorter reactive time. However, other parameters, including travel speed and powder mass flow rate, also affect the deposition process and the geometry of the deposition [6]. Moreover, there are interdependencies between these parameters.

In addition, since process parameters also affect the microstructure, porosity and mechanical properties, it is important to consider how these may change. The literature gives an insight into the effect of process parameters and interrelated physical phenomena on the properties of DED parts. Among others, Sciammarella and Najafabadi [7] showed that consistent microstructures and microhardness in components produced by DED-LB/Powder can be achieved with specific ratios of powder mass flow rate to travel speed, because of the dependency between the two factors. Additionally, the environmental conditions during fabrication must be controlled to minimize defects and ensure process stability. Typically, DED processes are conducted within an inert and controlled atmosphere to limit oxidation and contamination, ensuring consistency in material properties and deposition quality. Despite these controlled conditions, the DED process remains highly complex, involving multiple physical phenomena occurring simultaneously, such as heat transfer, phase transitions, fluid dynamics, and material solidification. Previous research has investigated the effects of various process parameters on the properties of components produced by DED. Aversa et al. [8] examined the influence of chamber conditions on the characteristics of morphology, geometry, and microstructure of the specimens. They stressed the importance of considering multiple metrics when evaluating deposition quality, including porosity and mechanical properties such as elongation and Young's modulus. Piscopo et al. [9] developed a hybrid finite element-experimental model to relate the height of AISI 316L single tracks produced through DED-LB/Powder to the energy density and powder feed rate, as a tool for process parameters optimization in geometry. Moheimani et al. [10] investigated the impact of substrate preheating on the microstructure, roughness, and mechanical performance of the AISI 316L produced by DED-LB/Powder. Aversa et al. [11] examined the effect of boundary conditions in the building chamber on the properties of additively manufactured components using the DED-LB/Powder process. Recently, Era et al. [12] employed machine learning techniques to predict the mechanical performance of DED-LB/Powder AISI 316L components by varying the process parameters, based on a limited data set.

This work aims to identify the key factors influencing deposition height and to validate a model that optimizes the powder feed rate without feedback control, ensuring the desired growth under specified process parameters. The model is derived from an investigation of the factors that influence the growth of deposition in DED, and the interdependence between energy density, tracks overlap, and powder mass flow rate. The analysis considers controllable factors in a DED system, as well as sources of noise, such as variations in environmental conditions, which are monitored to evaluate their potential impact. With the aim of identifying the active factors in DED to ensure correct deposition growth, screening experiments were conducted using a factorial design approach, which enables systematic assessment of key parameters while optimizing the number of experimental runs. As case study, the process window is identified for AISI 316L in the DED system available to the research. Parameters values in the process window guarantee consistent part quality in terms of effective growth, density, porosity and hardness.

1.1 Modeling the deposition mechanics of the DED process

To intercept the parameters to be included in the analysis, a theoretical model of the deposition of overlapping tracks in DED-LB/Powder has been developed. The Eulerian approach has been preferred for modelling the deposition, as it simplifies both the equations and the modeling process. In this approach, a Control Volume (CV) is defined. The CV is centered at the Stand-off Distance (SoD) from the head nozzle and is geometrically defined as a cylinder. It moves with an absolute velocity equal to the travel speed (v), and trajectory as the deposition path. The dimension of the CV is so that to include the powder stream converging into the melt pool and the melt pool itself. In the absence of external disturbances, powder particles entering the melt pool area are considered to contribute to the deposited material ($\dot{m}_{\mathrm{deposit}}$). Instead, powder particles that are not incorporated into the deposit are regarded as lost ($\dot{m}_{\mathrm{loss}}$). The upper surface of the CV is the area through which the powder is delivered, while the lateral surfaces are crossed outwards by the powder lost during the process as depicted in Fig. 1. Using the Alternate

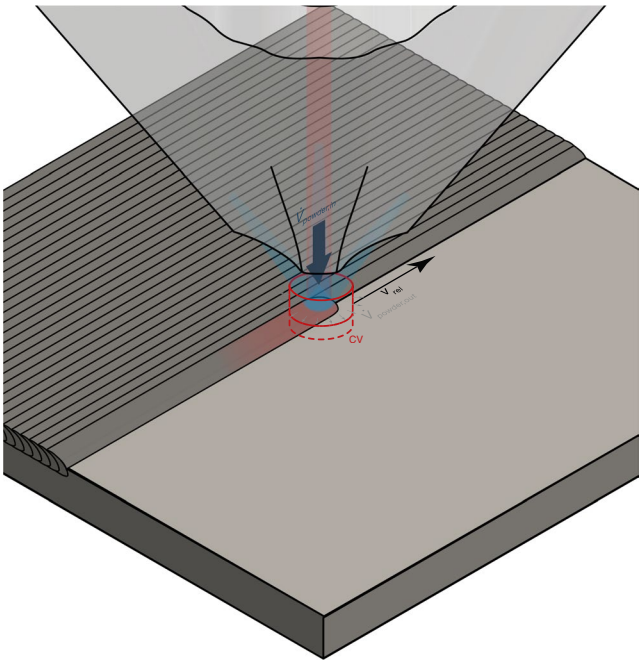


Fig. 1 Control Volume (CV) of the DED process

Reynolds Transport Theorem (RTT) with a non-fixed CV [13], the conservation of the mass can be expressed by:

$$\frac{d\,M_{sys}}{dt} = \frac{d}{dt}\int_{CV} \rho\, dV + \int_{CS} \rho \overrightarrow{v}_{rel} \cdot \overrightarrow{n}\, dA \tag{1}$$

where, M_{sys} represents the total powder mass that is converted in bulk material and $\frac{dM_{sys}}{dt}$ corresponds to the mass deposition rate, $\dot{m}_{\text{deposit}}$. The velocity term $\overrightarrow{v}_{\text{rel}}$ denotes the relative velocity between the CV and the powder flows crossing the control surfaces, CS. In a steady state condition, the volume integral can be disregarded. Therefore, the mass supplied to the system can be expressed as the difference between the powder that enters and exits the control volume:

$$\frac{dM_{\text{sys}}}{dt} = \int_{CS} \rho\, \overrightarrow{v}_{rel} \cdot \overrightarrow{n}\, dA = \rho_{\text{powder}} \dot{V}_{\text{powder,in}} - \rho_{\text{powder}}\, \dot{V}_{\text{powder,out}} \tag{2}$$

As a further simplification, a dimensionless coefficient, κ, is introduced as the ratio of the powder mass flow rate, $\dot{m}_{\text{powder}}$, to the deposition rate, $\dot{m}_{\text{deposit}}$. It should be noted that κ is the reciprocal of the powder capture efficiency (η_p), while accounting for the surplus powder necessary for consistent deposition [14].

$$\kappa = \frac{\dot{m}_{\text{powder}}}{\dot{m}_{\text{deposit}}} = \frac{\rho_{\text{powder}}\, \dot{V}_{\text{powder,in}}}{\rho_{\text{powder}}\, \dot{V}_{\text{powder,out}}} = \frac{1}{\eta_p} \tag{3}$$

Provided that the powder density is equal to the bulk density of the deposit, the relationship can be expressed in terms of volume rate of the deposit:

$$\dot{V}_{\text{powder,in}} = \kappa\, \dot{V}_{\text{deposit}} \tag{4}$$

Ideally, the deposit volume rate, $\dot{V}_{\text{deposit}}$, can be assumed equal to the cross-sectional area of the track multiplied by the travel speed. The cross-sectional area results from the process parameters adopted, including the deposition strategy, and could be roughly approximated as a rectangle with width W and height H:

$$\dot{V}_{\text{deposit}} = v\, A = v\, W\, H \tag{5}$$

The deposit width, W, can significantly vary according to the process parameters and energy density: however, at first approximation, it is considered equal to the laser focus diameter, D. Overlap ratio, O_e, is introduced here as complement fraction of the ratio of the hatching distance, d, between two consecutive tracks (see Fig. 2a), to the laser spot diameter [15]:

$$O_e/\% = \left(1 - \frac{d}{D}\right) 100 \tag{6}$$

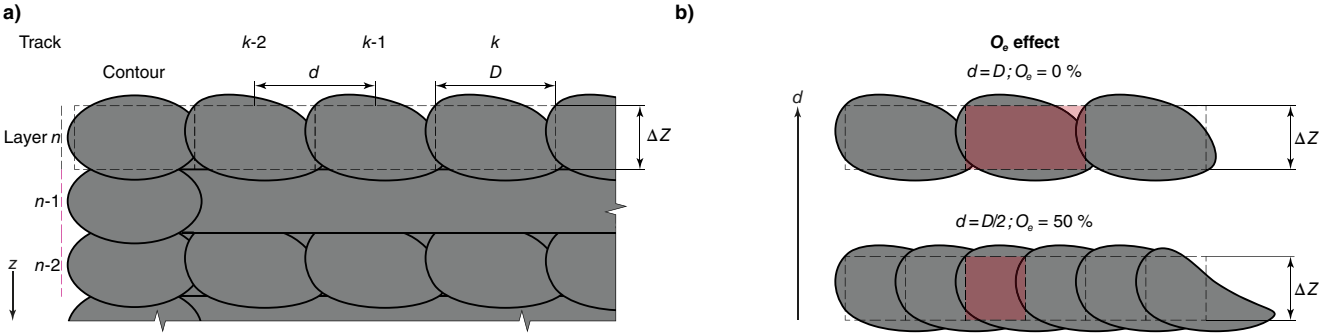


Fig. 2 (**a**) Geometric parameters of the deposition, and (**b**) O_e effect

The O_e effect is depicted in Fig. 2b: with 0% O_e, the laser scans do not overlap at all; with 50% overlap, each layer is scanned twice (except for the contour area). This attribute transforms O_e into an intuitive applicable factor. In case of overlap, to maintain the same track cross-sectional area, less powder is needed because part of the previous track is remelted. In the model, to account for overlap, the deposition rate is adjusted by correcting the deposit volume rate with the O_e value.

Rearranging the previous equations and linking the input characteristics of the system under examination, while assuming that $W=D$, the formula for the powder mass flow rate is derived as follows:

$$\dot{m}_{\text{powder}} = \rho_{\text{powder}}\ \kappa\ v\ H\ D\,(1 - O_e) \tag{7}$$

From Eq. 7, it can be observed that the $\dot{m}_{\text{powder}}$ is directly related, among process parameters, to the v, the desired height H, to the percentage overlap O_e, as well as by D, that is system-dependent, and, finally, the κ. It is worth noting that the laser power, even if not explicitly included here, has an indirect effect since it influences the track cross-section size [16].

2 Design of the factor screening experiment

In the experimental analysis, the focus gravitates towards an optimization of the powder stream without a feedback system for the deposit height. The aim is to quantify the powder to be delivered to the melt pool to ensure a track height corresponding to the Z-increment of the deposition head, ΔZ, at each subsequent layer. Thus, an experimental campaign was designed to verify the adequacy of the model in assessing the correct amount of powder flow to be delivered under a given set of deposition parameters.

2.1 Responses

When designing a factor screening experiment, the first step is to carefully select the responses to analyze. Besides the actual height of the deposition, which is of primary interest in this work, other response variables related to the bulk properties of the part were selected, specifically porosity and hardness, as suggested by Tan et al. [17]. Porosity provides information about the effectiveness of the process parameters and their interactions during the deposition, with low porosity indicating that the process parameters interacted effectively. Microhardness was selected as a response variable as it is linked to the thermal history of the process, the microstructure, and mechanical properties.

2.2 Factors and levels

The Eq. 7 evidences the interdependence of $\dot{m}_{\text{powder}}$ with v, D and O_e, as well as the coefficient κ, the dimensionless parameter introduced to account for surplus powder. The first factor considered in this study is ΔZ, which is the Z-increment of the deposition head for each new layer. Other factors considered in this study are the O_e, the κ, and the specific energy density, $E = \frac{P}{vD}$, which aggregates process parameters P and v, as well as the laser focus diameter D [18]. Notably, E is linked to the resulting microstructure and presence of defects, such as gas entrapped porosity, keyholes, lack-of-fusion, and delamination [19]. Although the variation of E can be achieved through various combinations of laser power and scanning speed, the laser power was kept constant in this study, assuming variable only the scanning speed. In practice, at a constant laser power, E is halved when the travel speed is doubled. Considering the inherent uncertainties associated with experimental errors, a conservative strategy was implemented that focused on extending the ranges of factor levels to include only the extreme values allowed by the DED system, namely the corner points of the factorial design. This methodology ensures thorough coverage and increases the robustness of the investigation.

3 Experimental setup

The following sections describe and discuss the primary components of the experimental setup, including the DED-LB machine and the feedstock powder. The environmental boundary conditions were monitored by a custom-designed system that integrates sensors and data acquisition tools. An in-depth description of the monitoring system resides in the Appendix A.

3.1 DED system

The Laserdyne 430 DED-LB system used in this research, provided by Prima Additive (Turin, Italy), has a deposition head integrated into a CNC system equipped with a roto-tilting table, enabling five-axis deposition. The deposition head houses four distinct nozzles tailored for powder flow, each presenting a nominal radius, r_{nozzle}, of (0.50 ± 0.01) mm. The system is equipped with a fiber laser capable of delivering a maximum power of 1 kW into a focused beam diameter of 2 mm. This DED-LB/Powder system is paired with an Optomec CS 150 (Albuquerque, NM, United States) powder feeding system. The latter consists of a metering rotating disk under a gravity hopper and powder conveyance by pressurized inert gas. In the case under study, employing

Table 1 DED system parameters datasheet

Parameter	Value
Building volume	$(585 \times 400 \times 500)$ mm^3
Laser type	Yb fibre laser
Wavelength	(1075 ± 3) nm
Beam diameter	(2.00 ± 0.01) mm
Standoff distance	8 mm
Carrier gas type	Argon
Power	(100 to 1000) W
Travel speed	(0 to 250) mm s^{-1}
$\dot{m}_{\text{powder}}$ $316L$	(0.2 to 22) g min^{-1}

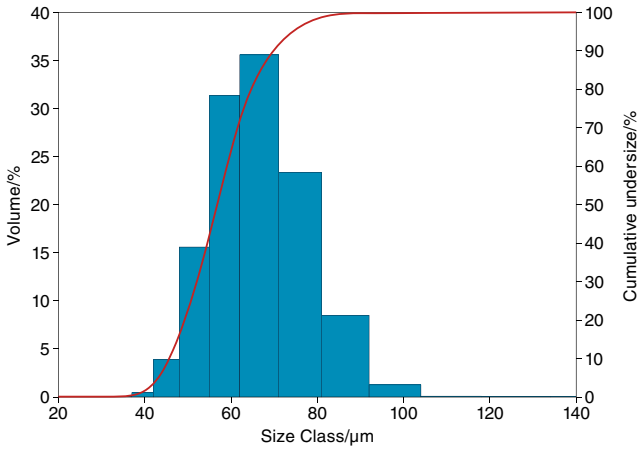


Fig. 3 Particle size distribution

AISI 316L powder and argon as carrier gas, the system achieves a maximum $\dot{m}_{\text{powder}}$ of 22 g min^{-1}. The specifics of the system used in this study are presented in Table 1.

3.2 Feedstock material

To ensure part quality, various aspects of the DED process should be considered. A key factor is the starting material, both in terms of the powder feedstock and the substrate. The composition, purity, and granulometry of the powder, as well as the metallurgical properties of the substrate, play a crucial role in determining the final properties of the part. This study used commercially available gas-atomized pre-alloyed AISI 316L stainless steel powder from Oerlikon (Freienbach, Switzerland) as the starting material. The particle size distribution of the powder was unimodal and gaussian, with D_{10}=49.2 μm, D_{50}=60.9 μm, and D_{90}=74.6 μm (see Fig. 3).

A scanning electron microscope micrograph of the as-received powder is presented in Fig. 4a, showing mainly spherical particles but some defects such as satellites, agglomerates, and elongated particles. The average density of the powder was calculated using a two-step approach. Initially, the mass of the powder was evaluated with a

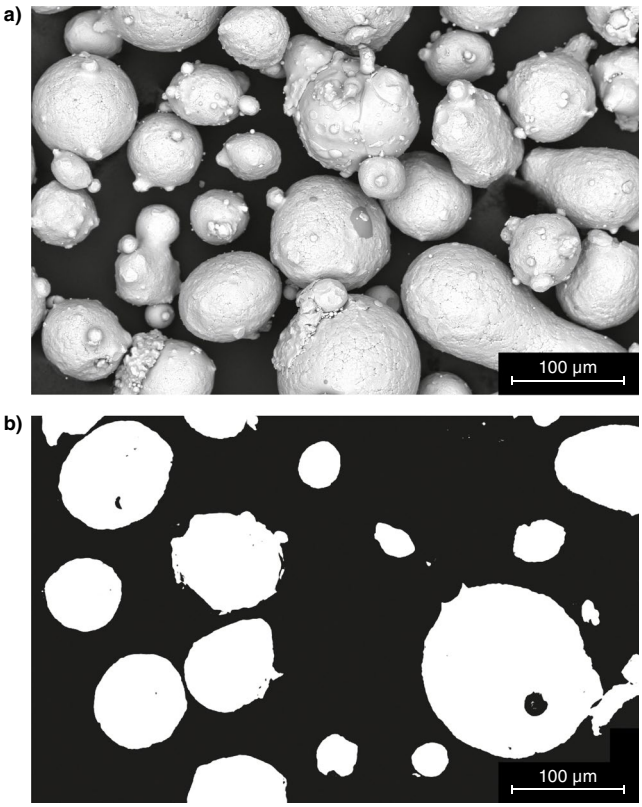


Fig. 4 (**a**) SEM micrograph of 316L powder, and (**b**) optical micrograph of cross-section of 316L powder

high-accuracy ABS 320–4 N balance by KERN (Gottlieb, Germany). Subsequently, the pycnometer Ultrapyc 5000 by Anton Paar (Graz, Austria) was used to evaluate the volume of the powder sample. This device applies an iterative method until it reaches a variance of 0.01%. These collective data allowed to determine an average density value of (7.896 ± 0.005)[1] g mm^{-3} at (20.000 ± 0.001) °C.

[1] A Type B uncertainty with a rectangular distribution was used for mass, while volume had a Type A uncertainty. In determining the combined uncertainty, degrees of freedom from volume measurements were utilized, leading to a coverage factor from the Student's *t*-distribution that ensured a 95% confidence interval for expanded uncertainty [20].

Table 2 Chemical composition of AISI 316L stainless steel powder

Composition/ wt%	C	Cr	Cu	Fe	Mn	Mo	Ni	*P*	S	Si	O	*N*
Standard [23]	0.030	16.00–18.00	0.75	Bal.	2.00	2.00–3.00	10.00–14.00	0.045	0.03	1.00	*	*
Nominal	<0.01	17.34	0.04	65.72	1.40	2.34	12.55	0.012	<0.010	0.49	0.03	0.08

The cross-section of the starting powder was then examined using the optical microscope DMI 5000 M by Leica Microsystems (Wetzlar, Germany) which revealed the presence of pores (as shown in Fig. 4b). The bulk properties of the powder were measured following ISO 4490 [21] for flowability and ISO 3953 [22] for tap density. The time required for 50.0 g of powder to pass through a Hall funnel was (15.26 ± 0.08) s, and the Carr's compressibility index was 8.3%, indicating excellent flowability. The standard range and nominal chemical composition are presented in Table 2.

3.3 Boundary conditions monitoring

While boundary conditions may be unmanageable, they remain measurable. During deposition, the monitoring system captured the air temperature and absolute humidity inside the construction chamber. These measurements were subsequently used as covariates in the analysis of covariance (ANCOVA) [24]. Moreover, the initial substrate temperature before each deposition was monitored through a K-type thermocouple. Due to its inherent limitations in precision, accuracy, and placement (fixed) on the substrate, the acquired temperature served mainly as a monitoring system rather than a covariate in the ANCOVA. The substrate retains residual heat post-deposition, potentially affecting the consistency of subsequent depositions. To uphold experimental consistency, the initiation of new depositions was ensured at a substrate temperature of 20 °C, with a permitted variance among trials no greater in absolute value than 5 °C.

3.4 Factor screening design

The factors under investigation are summarized alongside their corresponding levels and symbolized by the coded factor levels as +1 (high levels) and −1 (low levels). The factor levels were selected ensuring that the calculated powder flow rates $\dot{m}_{\mathrm{powder}}$ always fall within the operational range of the system, [0.2, 22.0] g min^{-1}. The design center from which factor levels were expanded was guided by the recommendation of the manufacturer for the AISI 316L (E = 53 J mm^{-2}). Following the approach of Salmi et al. [25], the laser power was set to P = 650 W and the layer increment to ΔZ = 0.50 mm. For the powder utilization factor κ, which must satisfy $\kappa \geq 1$, levels were chosen based on an estimated 25% loss in powder capture, namely κ = 1.25 (η_p = 0.80) and κ = 1.40 (η_p = 0.71). The O_e was set to 0% and 50% to evaluate the effect of the absence versus the presence of track overlap on the responses. The factor levels explored in this study are reported in Table 3.

For each set of factors, the corresponding values of travel speed and powder mass flow rate were calculated as follows:

Travel speed: the v value set in each experimental run was set based on the value of E and O_e as $v = P/(E(1-O_e)D)$. The introduction of this (operative) formulation was motivated by a further consideration. E is the energy transmitted to the layer during deposition, irrespective of overlap. However, as mentioned before, if an O_e by 50% is utilized, the laser would traverse the same point twice for each layer. To have the same energy transmitted to the layer, this would consequently lead to a reduction by half of specific energy density E. The actual energy density E_{a} is thus defined as the input energy density delivered during deposition of overlapped deposits and is quantified as.

$$E_a = E\,(1 - O_e) \tag{8}$$

Powder mass flow rate $\dot{m}_{\mathrm{powder}}$ was calculated using Eq. 7. The $\dot{m}_{\mathrm{powder}}$ was regulated in the feeder system by varying the rotational speed of the metering disk at a constant $\dot{V}_{\mathrm{Ar}}$ level of 5 L min^{-1}.

Square-based parallelepiped with dimensions of (12 × 12 × 15.6) mm³ were deposited onto platforms measuring (110 × 110 × 10) mm^3 in AISI 316L. The nominal total height of 15.6 mm was chosen for easier analysis, as it is divisible by the chosen ΔZ values. The specimens were

Table 3 Analyzed factor levels

Coded factor	Factor	Low coded level	High coded level	Low natural level	High natural level
x_1	E	−1	1	46 J mm^{-2}	60 J mm^{-2}
x_2	κ	−1	1	1.25	1.40
x_3	O_e	−1	1	0%	50%
x_4	ΔZ	−1	1	0.4 mm	0.6 mm

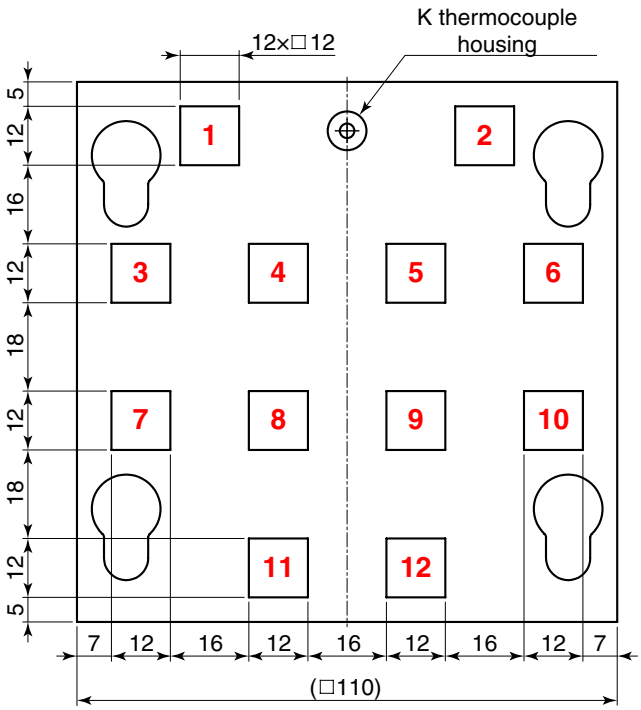


Fig. 5 Layout of the twelve (12 × 12 × 15.6) mm³ specimen positions on the build platform (110 × 110 × 10) mm³

fabricated using a raster scanning strategy without contour, and rotation of the scan pattern by 90° at each new layer. Each platform can accommodate 12 specimens; their positions are shown in Fig. 5. The 2^4 full factorial design with 3 replicates was divided into 4 blocks. Blocking was introduced to eliminate the effect of the change in substrate platform on the analysis. As a rule of thumb, high order interactions were used to construct blocks. Moreover, since this study primarily aims at factor screening, analyzing up to the two-way interaction suffices. For a 2^4 design with 2^2 blocks of resolution III, a two-way interaction between two factors remains confounded with blocks. A pivotal choice involved confounding the two-way interaction $\kappa \cdot O_e$. This was motivated by prior knowledge and experimental evidence from comparable settings, in which κ and O_e have not shown any significant interaction [26]. Accordingly, we assume O_e to be independent of κ in this screening step. This strategy follows the effect sparsity principle and keeps main effects identifiable; if needed, de-aliasing can be performed in follow-up experiments.

3.5 Response measuring procedure

The height of each specimen was directly measured using the EquatorTM 300 precision gauging system by Renishaw (Wotton-under-Edge, United Kingdom). Given that the DED-LB process inherently induces residual stresses, which may lead to distortion of the substrate, each specimen

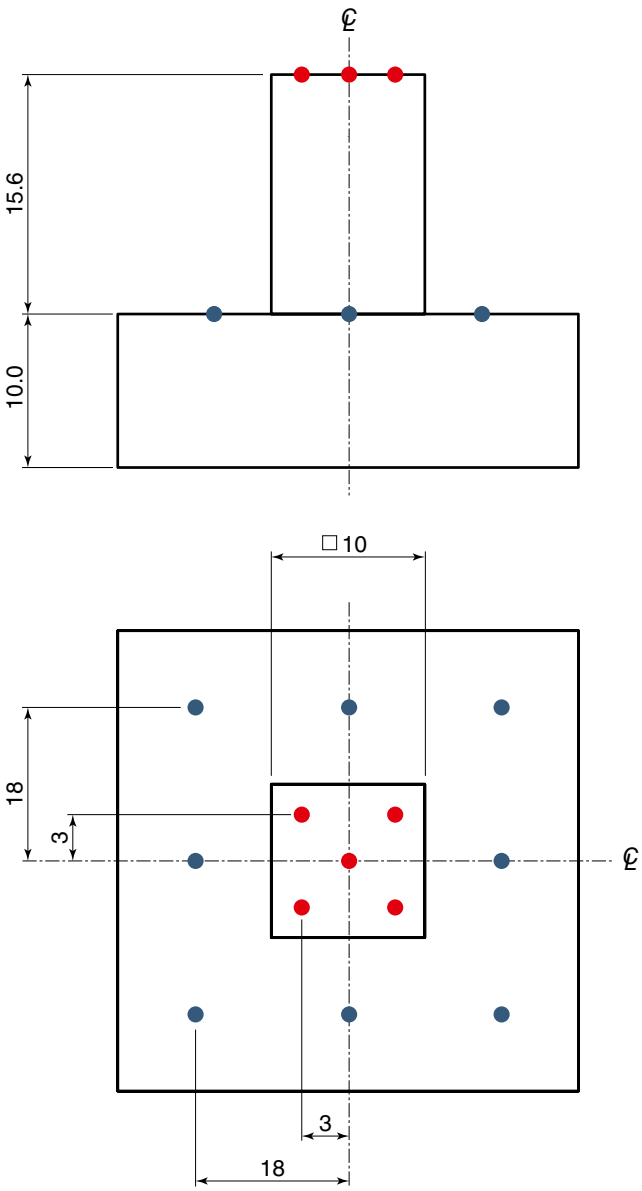


Fig. 6 Measurement locations: five red points on the specimen top surface and eight blue points on the substrate surface

was measured locally to minimize the influence of both local and global substrate deformations. Thus, for each specimen, the substrate plane was recreated using eight measurements made with the touch probe on the platform, which were spread evenly around the specimen (measurement locations are illustrated in Fig. 6). The mean distance of five measurements uniformly distributed on the top surface was used to determine the height.

Following height measurements, specimens were separated from the platform using wire electrical discharge machining (wire-EDM) and then reduced to volumes of 1 cm³ for density evaluation Fig. 7a. A BRILLANT 220 precision cutting machine by QATM (Mammelzen, Germany)

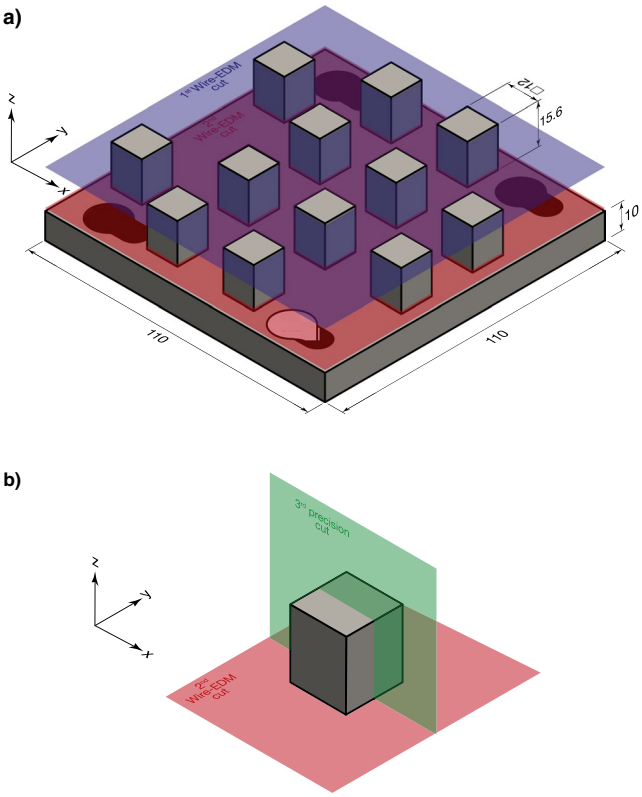


Fig. 7 Specimen preparation: (a) wire-EDM cuts along planes parallel to the xy-plane; (b) specimens halved using a precision cutting machine

was used Fig. 7b. Each volume was thoroughly polished and cleaned to avoid surface oxidation impacts on subsequent evaluations. The density of the specimens was measured using the ABS 320–4 N precision balance and the Ultrapyc 5000 pycnometer. Next, the specimens were split using the precision cutting machine and embedded in acrylic resin. After following to standard procedures, the specimens were treated to achieve a mirror-like surface, which facilitated porosity measurements through image analysis.

Subsequently, 25 random micrographs were captured from each specimen using the DMI 5000 M optical microscope by Leica (Wetzlar, GER) with a 100× magnification factor. The subsequent analysis was conducted using ImageJ, a public domain image processing tool endorsed by the National Institutes of Health, known for its adaptability and comprehensive utility in scientific image analysis.

Finally, the microhardness of the specimens was measured using the DHV-1000 digital micro-Vickers instrument by JVS (Licheng District, Jinan, China). For each specimen, five measurements were taken at the bottom (2 mm from the substrate) and the top (12 mm from the substrate), using a load of 0.5 kgf and a dwell time of 15 s (HV/0.5/15), following ASTM [27] recommendations for minimal spacing between each indentation.

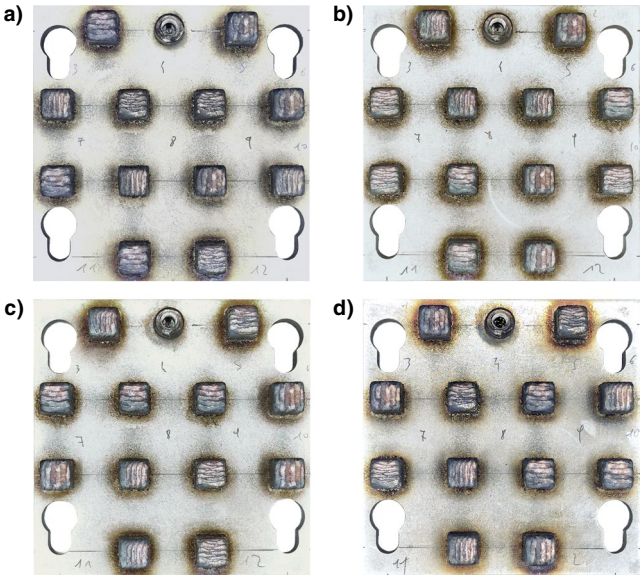


Fig. 8 48 specimens produced on four substrates (blocks): (a) Block 1, (b) Block 2, (c) Block 3, and (d) Block 4

4 Results

All specimens within a block were deposited on a single day, and the resulting builds are shown in Fig. 8. For each response, the ANCOVA was performed, excluding the two-way interaction involving ($\kappa \cdot O_e$) since it is totally confounded with Blocks. The statistical analysis was conducted using MINITAB® 20.1.3 software (Gaithersburg, MD, USA). Table 4 presents the experiment data.

4.1 Height assessment

Most samples reached the desired height, with a mean height of 101.4% and an overall Standard deviation (S) of 2.95% across the full dataset. At the specimen level, the mean within-specimen S is approximately 0.4%, corresponding to about (15.82 ± 0.06) mm. Results from the ANCOVA regarding height are presented in Table 5. The model achieved an $R^2(adj)$ of 87.53%. Residual analysis revealed a predominantly normal distribution.

A thorough examination reveals no covariate significantly influencing the response within the studied ranges. Notably, the Blocks are found to be statistically not significant. Approximately 74% of data variability, Sum of Squares (SS), can be attributed to the main effects E, κ, O_e, ΔZ, depicted in the main effect plot in Fig. 9. Among the investigated factors, ΔZ emerges as the most important factor, accounting for about 44.5% of the variability, followed by O_e (25.9%). Additionally, the two-way interaction plots are presented in Fig. 10.

Table 4 Experiment data

Std O.	Run O.	Plat. Pos.	Block	E/(J mm^{-2})	κ	O_e/%	ΔZ/mm	Height/%	Density/(g cm^{-3})	Porosity/%	Hardness/HV	T_T[a]/°C	T_A/°C	H_A/(g m^{-3})
1	35	3	1	60	1.40	0	0.4	102.01	7.907	0.037	163	22.2	27.9	6.9
2	29	12	1	46	1.25	50	0.4	105.89	7.895	0.016	167	18.6	27.1	6.6
3	28	10	1	46	1.40	0	0.6	98.88	7.917	0.064	170	17.4	27.0	6.7
4	25	1	1	60	1.25	50	0.6	100.20	7.916	0.032	164	16.6	26.3	6.5
5	27	4	1	60	1.40	0	0.4	103.79	7.924	0.053	168	22.2	26.9	6.6
6	33	2	1	46	1.25	50	0.4	105.61	7.897	0.034	164	22.0	27.9	6.8
7	31	7	1	46	1.40	0	0.6	97.88	7.895	0.062	167	20.9	27.4	6.7
8	26	8	1	60	1.25	50	0.6	100.19	7.915	0.012	159	21.5	26.6	6.6
9	34	5	1	60	1.40	0	0.4	105.65	7.883	1.670	170	22.0	28.0	6.8
10	30	9	1	46	1.25	50	0.4	106.40	7.882	0.011	161	18.0	27.2	6.6
11	32	6	1	46	1.40	0	0.6	98.34	7.913	0.018	168	15.1	27.7	6.8
12	36	11	1	60	1.25	50	0.6	101.39	7.902	0.045	163	20.0	28.1	7.0
13	45	9	2	46	1.25	0	0.4	101.94	7.950	0.018	168	24.8	27.4	9.2
14	39	2	2	60	1.40	50	0.4	105.74	7.957	0.681	169	15.4	26.5	8.9
15	40	12	2	60	1.25	0	0.6	96.50	7.946	0.024	162	22.3	26.7	8.9
16	37	6	2	46	1.40	50	0.6	98.59	7.890	0.014	161	*	25.5	8.7
17	43	10	2	46	1.25	0	0.4	99.60	7.958	0.021	169	16.0	26.9	9.1
18	44	4	2	60	1.40	50	0.4	106.33	7.963	0.180	169	17.4	27.2	9.2
19	38	3	2	60	1.25	0	0.6	95.44	7.960	0.012	163	16.3	26.1	8.8
20	41	11	2	46	1.40	50	0.6	100.52	7.961	0.020	165	18.4	26.7	8.8
21	47	5	2	46	1.25	0	0.4	101.58	7.958	0.051	168	17.6	27.5	9.1
22	48	7	2	60	1.40	50	0.4	103.90	7.947	0.463	166	19.7	27.4	9.1
23	46	1	2	60	1.25	0	0.6	96.80	7.951	0.066	168	24.8	27.5	9.1
24	42	8	2	46	1.40	50	0.6	100.60	7.965	0.147	170	19.0	26.9	8.9
25	1	11	3	46	1.40	0	0.4	101.16	7.928	1.032	166	24.6	25.3	7.2
26	10	5	3	60	1.25	50	0.4	105.28	7.934	0.069	161	20.0	27.1	6.9
27	9	6	3	60	1.40	0	0.6	98.28	7.926	0.009	166	22.9	26.8	6.8
28	6	3	3	46	1.25	50	0.6	97.79	7.916	0.021	167	23.1	26.5	6.9
29	7	7	3	46	1.40	0	0.4	99.78	7.909	1.305	170	19.0	26.6	6.8
30	12	4	3	60	1.25	50	0.4	106.03	7.936	0.024	160	21.4	27.1	7.0
31	3	2	3	60	1.40	0	0.6	101.25	7.933	0.084	167	21.2	26.3	7.0
32	11	10	3	46	1.25	50	0.6	99.35	7.928	0.329	170	22.8	27.2	6.9
33	8	1	3	46	1.40	0	0.4	101.68	7.924	0.050	172	19.9	26.9	6.9
34	5	12	3	60	1.25	50	0.4	103.92	7.939	0.017	166	18.8	26.5	6.9
35	2	9	3	60	1.40	0	0.6	99.16	7.926	0.051	165	*	25.9	7.1
36	4	8	3	46	1.25	50	0.6	98.63	7.936	0.033	169	18.9	26.5	6.9
37	24	6	4	60	1.25	0	0.4	103.03	7.912	0.015	166	19.1	26.6	6.5
38	13	3	4	46	1.40	50	0.4	104.08	7.949	0.016	165	*	24.9	6.9
39	21	12	4	46	1.25	0	0.6	98.28	7.925	0.036	169	16.0	26.1	6.4

Table 4 (continued)

Std O.	Run O.	Plat. Pos.	Block	E/(J mm^{-2})	κ	O_e/%	ΔZ/mm	Height/%	Density/(g cm^{-3})	Porosity/%	Hardness/HV	T_T^a/°C	T_A/°C	H_A/(g m^{-3})
40	23	4	4	60	1.40	50	0.6	102.57	7.923	0.010	162	17.1	26.2	6.6
41	14	8	4	60	1.25	0	0.4	100.13	7.922	1.116	167	17.8	25.4	7.0
42	16	10	4	46	1.40	50	0.4	105.56	7.939	0.016	167	18.7	25.7	6.8
43	20	9	4	46	1.25	0	0.6	99.14	7.914	0.195	172	16.9	26.2	6.5
44	19	5	4	60	1.40	50	0.6	102.58	7.930	0.045	171	20.6	26.2	6.5
45	18	11	4	60	1.25	0	0.4	101.78	7.919	0.767	164	17.3	26.1	6.6
46	15	7	4	46	1.40	50	0.4	103.81	7.941	0.025	164	14.2	25.6	6.8
47	22	2	4	46	1.25	0	0.6	97.92	7.930	0.028	168	15.8	26.2	6.5
48	17	1	4	60	1.40	50	0.6	102.21	7.929	0.021	168	18.4	25.8	6.6

[a]Some values are missing and are indicated by (*) in the table

A reduced model was obtained using the standard stepwise methodology for linear, quadratic and interaction terms. A non-hierarchical approach was employed to maintain a more conservative model, with a 10% *SL* as the Alpha-to-Enter and to Remove. The overall metrics of the model, including an S value of 1.1, an $R^2(adj)$ of 87.3%, and an $R^2(pred)$ of 83.2%, highlight the robustness of the developed model. The analysis of the residuals supports this, revealing no significant anomalies or signs of lack-of-fit (LOF). The regression coefficients are detailed in Table 6, presented in coded units and averaged across blocks.

Lastly, contour plots with isolines representing the response are shown in Fig. 11. The plots are divided into low and high levels of O_e. These plots show a significant zone around the 100% height value, consistent with the goal of the study. The average response of specimens constructed with a 50% O_e is higher than those constructed without overlapping (O_e = 0%). However, the response trend is consistent across both construction strategies.

4.2 Density assessment

After the polishing procedure for density assessment, the specimens exhibited volumes closely aligned within the range of (0.906 ± 0.061) cm³. The average measured density was (7.927 ± 0.006) g cm^{-3}, indicating negligible variation in density across the sets of process parameters used. This result proves that the model was adequate in achieving full dense specimens. To compare part density with the density of the fresh powder, a two-sample *t*-test was conducted. The null hypothesis stated that the powder density is lower to that of the specimen, the hypothesis is rejected with a *p*-value lower than 0.01% (see Fig. 12).

4.3 Porosity assessment

Following the density measurements, the specimens were sectioned, mounted, and polished to enable porosity evaluation. The porosity distribution is positively skewed, ranging from (0.01 to 1.67) %, with a mean of 0.19%, a median of 0.03%, and a skewness of 2.62. To address the strictly non-negative data, the Box-Cox method was chosen with a $\lambda = -0.5$ obtained through iterative method. However, the model generated through ANCOVA did not achieve the expected significance levels, rendering it unusable for predictive purposes. Despite this, further analysis of individual specimens provided noteworthy insights. Among the analyzed samples the sample that exhibited the lowest porosity, with a value of 0.01%, is shown in Fig. 13a. Conversely, the sample that recorded the highest porosity, reaching 1.67%, is illustrated in Fig. 13b. It is important to

Table 5 ANCOVA for height/%. Standard deviation of the residual, *S*, of 1.0, an $R^2(adj)$ of 87.53%, and an $R^2(pred)$ of 75.41%

Source	*df*	Contribution/%	Adj *SS*	Adj *MS*	*F*	*p*-value/%
Model	**14**	**91.25**	**375.413**	**26.815**	**24.56**	**<0.1**
Covariates	2	4.32	4.407	2.204	2.02	14.9
T_A	1	2.05	4.044	4.044	3.70	6.3
H_A	1	2.27	0.990	0.990	0.91	34.8
Blocks	3	8.53	5.462	1.821	1.67	19.3
Linear	**4**	**74.43**	**304.783**	**76.196**	**69.79**	**<0.1**
E	**1**	**1.61**	**8.211**	**8.211**	**7.52**	**1.0**
κ	**1**	**2.47**	**12.820**	**12.820**	**11.74**	**0.2**
O_e	**1**	**25.85**	**95.684**	**95.684**	**87.64**	**<0.1**
ΔZ	**1**	**44.49**	**185.106**	**185.106**	**169.54**	**<0.1**
2-Way Interaction	**5**	**3.96**	**16.296**	**3.259**	**2.99**	**2.5**
$E \cdot \kappa$	**1**	**1.64**	**6.859**	**6.859**	**6.28**	**1.7**
$E \cdot O_e$	1	0.05	0.196	0.196	0.18	67.4
$E \cdot \Delta Z$	1	0.12	0.416	0.416	0.38	54.1
$\kappa \cdot \Delta Z$	**1**	**1.15**	**4.660**	**4.660**	**4.27**	**4.7**
$O_e \cdot \Delta Z$	1	1.01	4.162	4.162	3.81	5.9
Error	33	8.76	36.030	1.092		
Total	47	100				

Highlighted terms have *p*-values $\leq \alpha = 5\%$

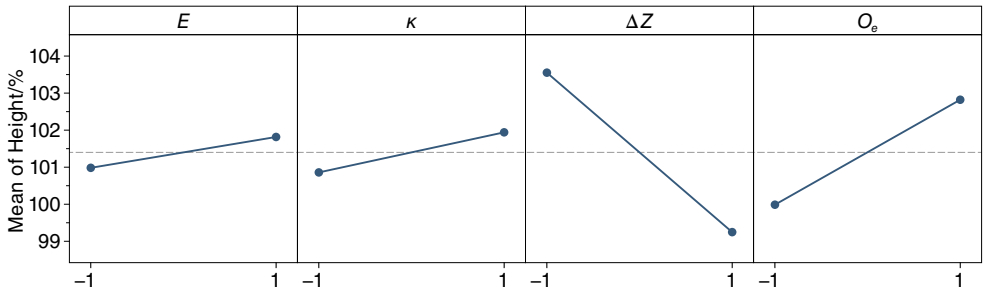


Fig. 9 Main effects factorial plots for height/%

highlight that both specimens were produced under identical energy input conditions (60 J mm^{-2}), O_e (0%) and κ (1.4), only varying the ΔZ value.

4.4 Hardness assessment

The average measured hardness was (166.3 ± 3.2) HV, indicating a limited variation in hardness across the sets of process parameters used. A comparative evaluation of hardness was conducted, focusing on the top five and bottom five points of each specimen. A two-sample *t*-test, assuming equal variances. The findings generally show lower hardness at the top compared to the bottom. This supports the observations made by several researchers [10, 28], who suggest that the higher cooling rate near the substrate results in a slightly finer microstructure and, therefore, increased hardness in these regions. An analysis of variance (ANOVA) was conducted to determine if the observed differences were affected by the selected factor levels or test assumptions. The ANOVA results confirmed that the variations in hardness could be attributed to the specifics of the process or test conditions, such as cooling rates, and not solely to differences within the selected factor levels.

Although the variance is quite narrow, an ANCOVA analysis was carried out on the mean values of each specimen to determine the presence of any effects of factors. The data analysis presented in Table 7. shows the significance of the model. The response is not notably impacted by either covariates or blocks. The residuals exhibit a normal distribution without any discernible patterns. The regression analysis yields an $R^2(adj)$ value of 30%, indicating that the majority of the variance can be attributed to the inherent variability of the investigated phenomena.

Despite the limited applicability of the model, it provides a qualitative wealth of information that will be deepened in future studies. From the main effects plots (Fig. 14) and the two-way interaction plots (Fig. 15), it can be inferred that an increase in energy input or constructing with overlap results in reduced micro-hardness. A similar effect is observed when increasing the surplus powder at higher energy input.

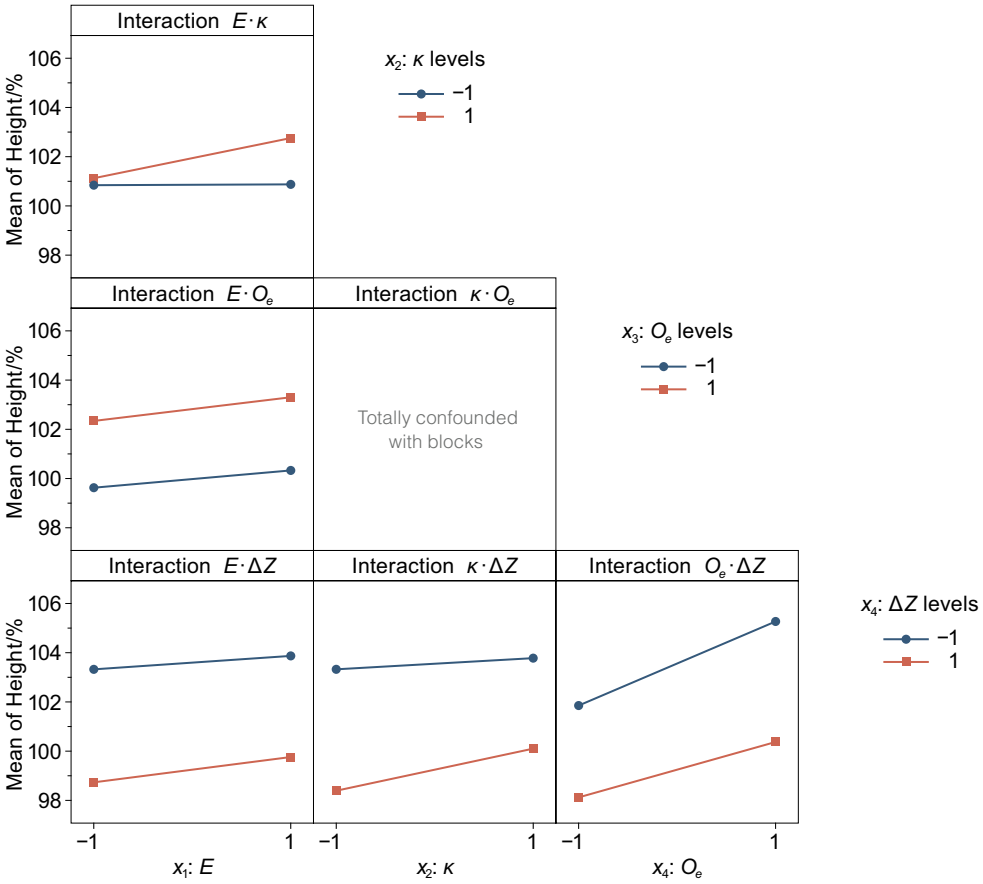


Fig. 10 Interaction plots for Height/%

Table 6 Estimates of the parameters for the Height reduced model in coded units, with terms averaged over blocks. The *SE* of the coefficients is 0.15

Variable	Parameter	Coefficient	*t*-value	*p*-value/%
Constant	β_0	101.40	666.15	<0.1
E	β_1	0.44	2.89	0.6
κ	β_2	0.45	2.95	0.6
O_e	β_3	1.40	9.20	<0.1
ΔZ	β_4	−2.13	−13.99	<0.1
$E \cdot \kappa$	β_{12}	0.50	3.29	0.2
$\kappa \cdot \Delta Z$	β_{24}	0.35	2.31	2.7
$\Delta Z \cdot O_e$	β_{43}	−0.28	−1.87	6.9

5 Discussion

The primary observation from the results of the screening analysis was that the model was effective in identifying the powder mass flow rate able to build a full dense specimen of desired height given a set of process parameters. A deeper analysis allowed to extract additional observations. First, looking at the main effects plots, the consequence of decreasing ΔZ values, which equates to build with a larger number of layers, leads to a noticeable increase in height, that mostly exceeded the target value. From Eq. 3, a lower ΔZ implies a lower $\dot{m}_{\text{powder}}$, that under stable condition reduces the laser power attenuation, thus enhancing the powder capture efficiency. The effect is indeed negligible at the single layer level, but it cumulates leading to the observed excess of material. An increase in height was observed also on specimens fabricated with an O_e of 50%. This suggests a non-linear effect of overlapping reduction to powder mass flow rate decrease. The κ factor emerges as another significant main effect. It is the evidence that supplying more powder to the melt pool leads to a height increment. Even if E is the least significant main effect, the $E{\cdot}\kappa$ interaction indicates that when E increases, the effect of κ is amplified. This is justified by a heightened capacity to melt and incorporate

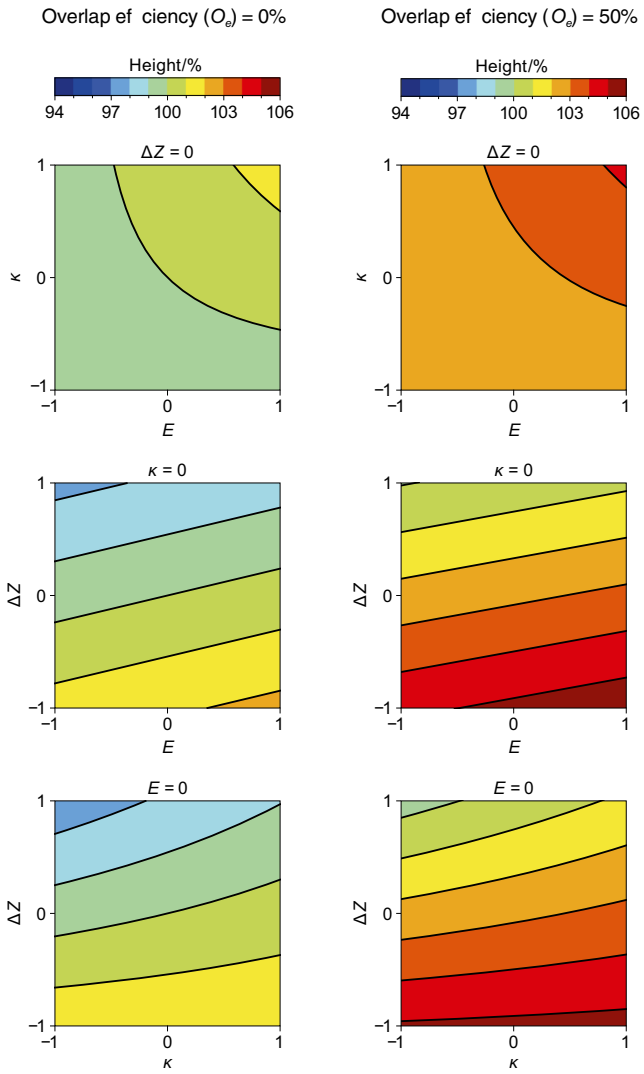


Fig. 11 Contour plots for the two levels of O_e for Height/%

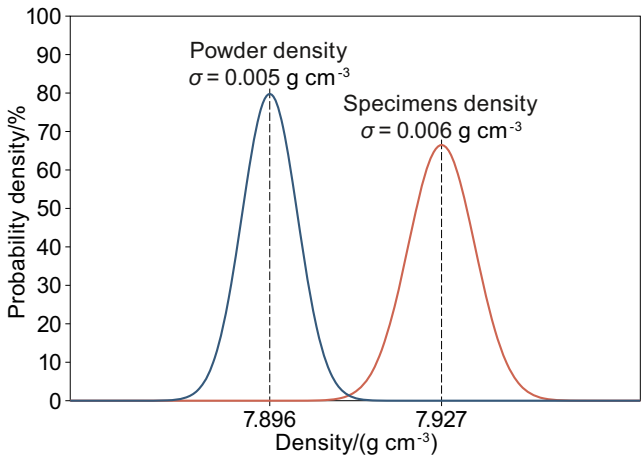


Fig. 12 Density comparison between powder and specimens

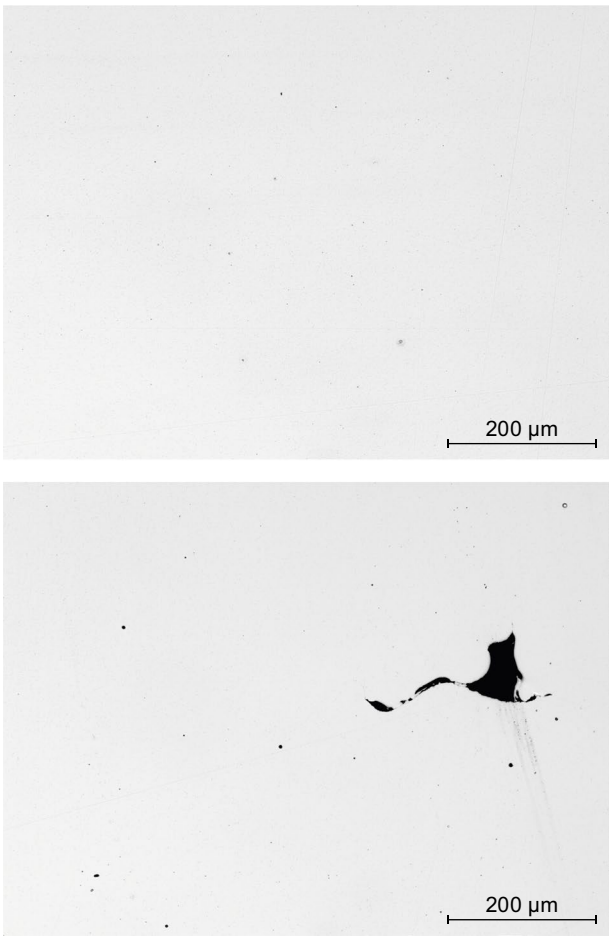


Fig. 13 Porosity in samples produced with E=60 J mm^{-2}, O_e = 0%, κ=1.4, and (**a**) ΔZ=0.6 mm (b) ΔZ=0.4 mm

more powder. Regarding the $E{\cdot}\Delta Z$ interaction, a decrease in height is observed with an increase in ΔZ (indicating fewer layers), but the effect is amplified for higher values of E. Higher energy lets each pass capture more powder, so with fewer passes the total captured powder is lower, amplifying the height loss. Although the $O_e{\cdot}\Delta Z$ interaction does not meet the chosen SL, it should be considered due to its borderline p-value. Similar to their main effects, an increase in height is observed as O_e and the number of layers intensify.

Shifting the focus to density, further insights can be drawn regarding process stability and material consolidation. Even if localized porosities were observed, all specimens within the specified process parameter window demonstrated uniform density. Due to the large sample size, the data effectively illustrates deviations from the mean density of the powder. The latter suggests that the porosity inherent to the powder is mitigated during the melting and solidification process.

Finally, the Hardness response was analyzed to understand the influence of process parameters on the mechanical properties of the specimens. Despite the differences in measured hardness were mostly attributed the inherent

Table 7 ANCOVA for hardness/(HV/0.5/15) The regression analysis yields an S value of 2.7 and an $R^2(adj)$ value of 30%

Source	*df*	Contribution/%	Adj *SS*	Adj *MS*	*F*	*p*-value/%
Model	**14**	**51.37**	**248.502**	**17.7502**	**2.49**	**1.6**
Covariates	2	0.40	15.966	7.9829	1.12	33.8
T_A	1	0.32	13.905	13.9051	1.95	17.2
H_A	1	0.08	0.430	0.4297	0.06	80.8
Blocks	3	9.26	32.492	10.8307	1.52	22.8
Linear	**4**	**29.26**	**132.091**	**33.0228**	**4.63**	**0.4**
E	**1**	**12.15**	**56.406**	**56.4056**	**7.91**	**0.8**
κ	**1**	**8.50**	**30.496**	**30.4963**	**4.28**	**4.7**
O_e	**1**	**8.26**	**41.836**	**41.8356**	**5.87**	**2.1**
ΔZ	1	0.35	1.839	1.8386	0.26	61.5
2-Way Interaction	5	12.46	60.263	12.0526	1.69	16.4
$E \cdot \kappa$	**1**	**5.50**	**29.485**	**29.4848**	**4.14**	**5.0**
$E \cdot O_e$	1	1.75	8.886	8.8860	1.25	27.2
$E \cdot \Delta Z$	1	1.78	8.075	8.0750	1.13	29.5
$\kappa \cdot \Delta Z$	1	2.36	11.331	11.3314	1.59	21.6
$O_e \cdot \Delta Z$	1	1.06	5.112	5.1119	0.72	40.3
Error	33	48.63	235.276	7.1296		
Total	47	100				

Highlighted terms have p-values $\leq \alpha = 5\%$

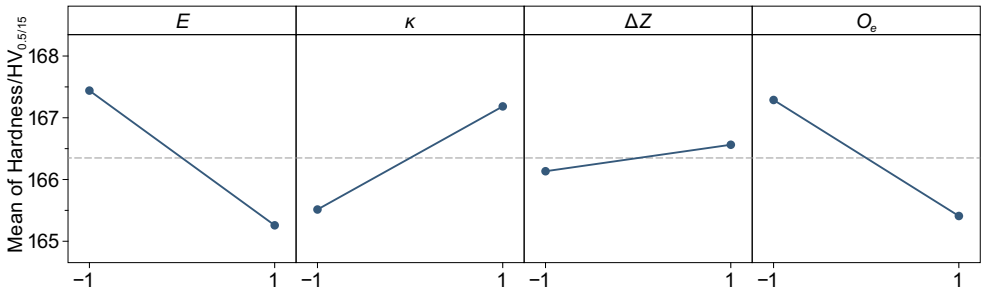


Fig. 14 Main effects plots for Hardness/(HV/0.5/15)

variability of the process, the four main effects also demonstrated significance, representing 29% of total variance of the model. Among these, E is the most influential, with a surge in E correlated to a reduction in Hardness. This phenomenon can be inferred to result from augmented energy intensifying heat distribution, subsequently influencing cooling rates and grain growth coefficients. Such modifications invariably induce alterations in the microstructure of the specimens, an outcome aligned with established theories such as the Hall-Petch law [29]. On another front, an escalation in the κ value diminishes the micro-hardness, likely stemming from mechanisms associated with thermal source attenuation. A decrease in micro-hardness becomes apparent when a 50% O_e value is adopted, justified by the repeated thermal cycle the material underwent. Analogously, an increase in layer count, due to the concurrent reduction in ΔZ, fosters reduced micro-hardness. Other controls that can influence microhardness include interlayer idle time, preheating, scan strategy and heat input distribution, cooling rate, and post-processing; these will be investigated in future work with expanded factor ranges.

6 Conclusion

This work examines the relationship between DED parameters and powder mass flow rate with the aim of optimizing powder delivery to the melt pool for accurate deposit production. Although developed without real-time height feedback, the approach is readily extendable to closed-loop control to enhance stability, consistency, and quality. The salient conclusions derived from the study are summarized as follows:

Height – The final height of the specimens depends mainly on the Z-increment (ΔZ) and, therefore, on the number of layers. A larger ΔZ (i.e., fewer layers for the same nominal height) results in a lower measured height. The parameters O_e, κ, and E also affect height. Models built at the two O_e levels show good precision in predicting height.

Density – The investigation revealed an average density of (7.927 ± 0.006) g cm^{-3} with limited dispersion, indicating a consistent and repeatable process in the tested ranges.

Porosity – The porosity distribution data were transformed to meet normality standards. However, the ANCOVA

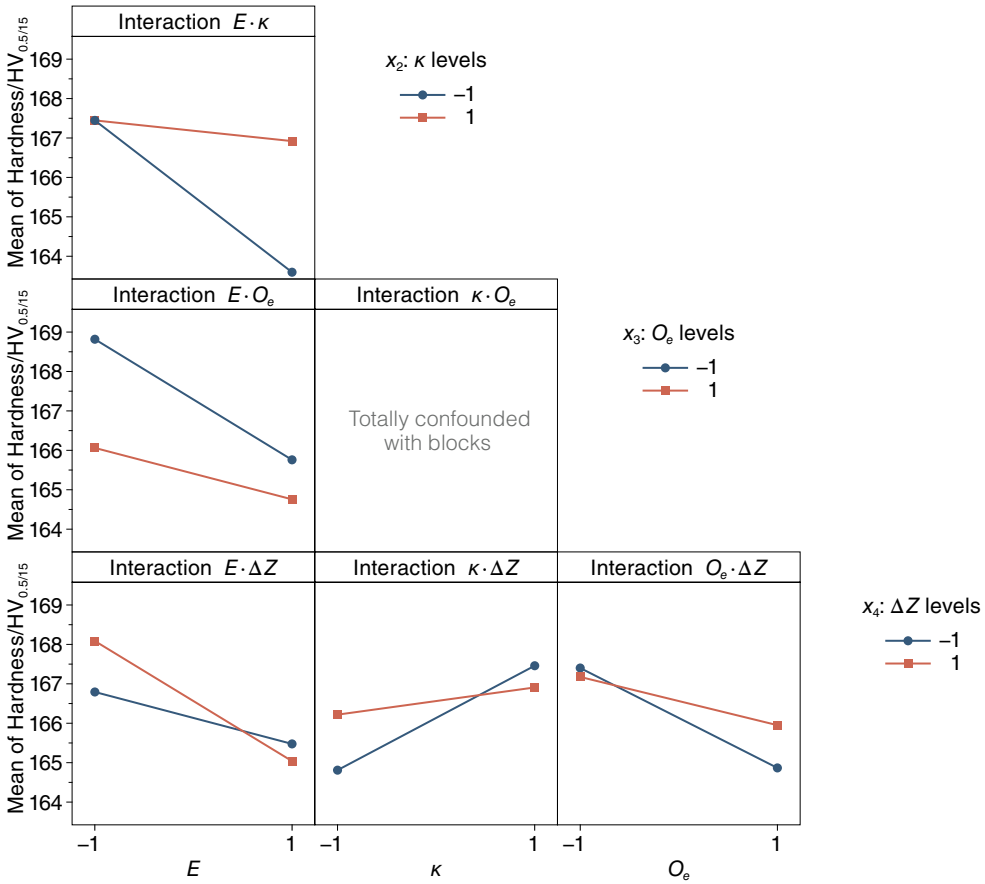


Fig. 15 Interaction plots for Hardness/(HV/0.5/15)

model proved insignificant post-transformation, and no correlation between density and porosity emerged. More specialized methods are needed to assess and model porosity.

Hardness – While multiple factors, such as E, κ, and O_e, influence micro-hardness, the established model accounts for only 30% of the observed variability. This finding suggests the potential presence of extraneous variables or inherent variations that are pivotal in shaping the hardness properties. Additional sources of variation are likely, and interactions matter, especially the interaction between E and κ.

The results show that height can be precisely controlled using the introduced powder feed method within the explored factor levels, while density and hardness appear to be relatively unaffected. Future research efforts will utilize the knowledge gained from this study to optimize powder delivery to achieve the desired percent height with minimum κ (that is maximum powder capture efficiency). The approach has clear industrial relevance, as it can support future in-situ adaptive control strategies in DED, reducing powder waste and improving process robustness. It is worth noting that the substrate material and geometry influence deposition outcomes through their effect on heat transfer and specimen temperature. Nonetheless, the relationship between powder mass flow rate and process parameters, in particular travel speed, retains general validity and can be tuned to the actual geometric constraints. Despite the promising results, it is imperative to note certain limitations that warrant attention in subsequent studies. The current conclusions are based on strong foundational hypotheses, which can be re-examined or relaxed in future research for more general applications. The scope of the study was limited to a single material and carrier gas type, but the encouraging results suggest the potential for more extensive investigation. The initial hypothesis that the density of the fabricated material equals that of the powder requires re-evaluation. Future models must account for the difference in density between the powder and the solid material to improve the accuracy and applicability of the deposition process.

Appendix

A custom monitoring system was developed to observe the BCs. The system incorporates two ESP32 microcontrollers, one for data acquisition and elaboration and the other for transmission as a web server. The Bosch BME280 sensor, which measures temperature, pressure, and relative humidity, meets the operating range requirements, accuracy, and environmental parameters for the chamber, as outlined in Table 8.

Table 8 Bosch BME280 characteristics [30]

Parameter	Symbol	Operating range	Unit	Accuracy
Temperature	T_A	−40 to +85	°C	±1.0
Pressure	p	300 to 1100	hPa	±1.0
Relative humidity	H_R	0 to 100	%	±0.12

The monitoring system is housed in an IP55 box within the construction chamber, with only the sensor exposed. A custom perforated nylon (PA12) part, produced using selective laser sintering, shields the sensor from powder dispersal.

Of the variables monitored, relative humidity depends on atmospheric pressure and temperature. Based on the authors' experience, determining absolute humidity is more advantageous and practically relevant. Absolute humidity can be derived from the quantity of steam contained in a mass unit of dry air, given by Cengel and Ghajar [31]:

$$H_A = \frac{0.622\, H_R\, P_V}{p - H_R\, P_V}$$

where H_A is the absolute humidity, HR is the relative humidity, p_v is the saturation vapour pressure which depends on the temperature, and p is the pressure. Furthermore, the measurement unit for the terms in the equation depend on the units of the desired result and must be chosen consistently among themselves. Additionally, the unknown term is saturated vapour pressure. The Clapeyron equation aids in determining the unknown saturated vapor pressure term, but the more manageable semi-empirical Antoine equation is preferred, derived from experimental data and Clapeyron's equation [32]. In this study, the three-parameter Antoine equation, valid between 0 °C and 100 °C, was employed:

$$\log_{10} p = A - \frac{B}{C + T}$$

where p is the vapour pressure in mmHg, T is the temperature in °C and $A = 7.96681$, $B = 1668.21$, and $C = 228$ are Antoine constants for water [33]

Data were collected at a 100 Hz sampling rate and processed using the Simple Moving Average, the most straightforward Moving Mean technique [34, 35]. With this method, it is possible to obtain the average of BCs during the duration of the experiment without the need to store all data, providing a more efficient and streamlined approach to data analysis. It should be noted that the model result was rounded to reflect the resolution of the sensor and the standard deviation of the regression

Acknowledgements The authors would like to acknowledge the Interdepartmental Centre for Integrated Additive Manufacturing (IAM@PoliTo) at the Politecnico di Torino, Torino, Italy.

Authors' contributions Pilagatti AN: investigation, methodology, writing - original draft; Vinčić J: investigation, methodology, writing - original draft; Atzeni E: formal analysis, writing - review & editing, resources; Salmi A: visualization, resources, writing - review & editing; Manfredi D: writing - review & editing.

Funding Open access funding provided by Politecnico di Torino within the CRUI-CARE Agreement. This work was supported by the regional project "4 ASSI-4 Assi Assieme per innovare", funded by Regione Piemonte with Grant POR FESR Piemonte 2014-2020 Piattaforma tecnologica di "Bando PiTeF".

Data availability The manuscript has no associated data. Data will be made available upon request.

Declarations

Ethical approval Not applicable.

Consent to publish Not applicable.

Consent to participate Not applicable.

Competing interests The authors declare that they have no known competing financial interests or personal relationships that could have influenced the work reported in this paper.

Open Access This article is licensed under a Creative Commons Attribution 4.0 International License, which permits use, sharing, adaptation, distribution and reproduction in any medium or format, as long as you give appropriate credit to the original author(s) and the source, provide a link to the Creative Commons licence, and indicate if changes were made. The images or other third party material in this article are included in the article's Creative Commons licence, unless indicated otherwise in a credit line to the material. If material is not included in the article's Creative Commons licence and your intended use is not permitted by statutory regulation or exceeds the permitted use, you will need to obtain permission directly from the copyright holder. To view a copy of this licence, visit http://creativecommons.org/licenses/by/4.0/.

References

1. ISO/ASTM 52900:2021(E) (2021) Additive manufacturing - general principles - fundamentals and vocabulary, American society for testing and materials (ASTM) International, West Conshohocken (USA)
2. Gibson I, Rosen D, Stucker B (2015) Additive manufacturing technologies: 3D printing, rapid prototyping, and direct digital manufacturing, 2nd edn. Springer, New York
3. Piscopo G, Iuliano L (2022) Current research and industrial application of laser powder directed energy deposition. Int J Adv Manuf Technol 119:6893–6917. https://doi.org/10.1007/s00170-021-08596-w
4. Liu M, Kumar A, Bukkapatnam S, Kuttolamadom M (2021) A review of the anomalies in directed energy deposition (DED) processes & potential solutions - part quality & defects. Procedia Manuf 53:507–518. https://doi.org/10.1016/j.promfg.2021.06.093
5. Garmendia I, Pujana J, Lamikiz A, Madarieta M, Leunda J (2019) Structured light-based height control for laser metal deposition. J Manuf Process 42:20–27. https://doi.org/10.1016/j.jmapro.2019.04.018

6. Ostolaza M, Urresti A, Arrizubieta JI, Lamikiz A, Ortiz M (2022) Cfd simulation for the modelling of the powder flow on continuous coaxial nozzles in the laser DED process. Procedia CIRP 111:282–286. https://doi.org/10.1016/j.procir.2022.08.022
7. Sciammarella FM, Najafabadi BS (2018) Processing parameter DOE for 316L using directed energy deposition. J Manuf Mater Process. https://doi.org/10.3390/jmmp2030061
8. Aversa A, Marchese G, Bassini E (2021) Directed energy deposition of aisi 316L stainless steel powder: effect of process parameters. Metals 11. https://doi.org/10.3390/met11060932
9. Piscopo G, Atzeni E, Salmi A (2019) A hybrid modeling of the physics-driven evolution of material addition and track generation in laser powder directed energy deposition. Materials 12. https://doi.org/10.3390/ma12172819
10. Moheimani SK, Iuliano L, Saboori A (2022) The role of substrate preheating on the microstructure, roughness, and mechanical performance of AISI 316L produced by directed energy deposition additive manufacturing. Int J Adv Manuf Technol 119:7159–7174. https://doi.org/10.1007/s00170-021-08564-4
11. Aversa A, Saboori A, Librera E, Chirico Mde, Biamino S, Lombardi M, Fino P (2020) The role of Directed Energy Deposition atmosphere mode on the microstructure and mechanical properties of 316L samples. Additive Manuf 34:101274. https://doi.org/10.1016/j.addma.2020.101274
12. Era IZ, Grandhi M, Liu Z (2022) Prediction of mechanical behaviors of L-DED fabricated SS 316L parts via machine learning. Int J Adv Manuf Technol 121:2445–2459. https://doi.org/10.1007/s00170-022-09509-1
13. Cengel Y, Cimbala J (2013) Fluid mechanics fundamentals and applications, 3rd edn. McGraw-Hill US Higher ED
14. Ancalmo C, Narra SP (2025) Prediction of the powder catchment efficiency and melt track height in laser directed energy deposition. J Manuf Process 137:207–220. https://doi.org/10.1016/j.jmapro.2025.01.039
15. Chang YY, Qiu JR, Hwang SJ (2022) Multi-objective optimization of directed energy deposition process by using Taguchi-Grey relational analysis. Int J Adv Manuf Technol 120:7547–7563. https://doi.org/10.1007/s00170-022-09210-3
16. Taghian M, Mazzucato F, Valente A, Saboori A, Iuliano L (2025) Optimizing CoCrNi single track geometry in directed energy deposition: a regression-based approach to laser power and scan speed control. Procedia CIRP 134:1035–1040. https://doi.org/10.1016/j.procir.2025.02.227
17. Tan ZEE, Pang JHL, Kaminski J, Pepin H (2019) Characterisation of porosity, density, and microstructure of directed energy deposited stainless steel AISI 316L. Addit Manuf 25:286–296. https://doi.org/10.1016/j.addma.2018.11.014
18. Shim D-S, Baek G-Y, Seo J-S, Shin G-Y, Kim K-P, Lee K-Y (2016) Effect of layer thickness setting on deposition characteristics in direct energy deposition (DED) process. Opt Laser Technol 86:69–78. https://doi.org/10.1016/j.optlastec.2016.07.001
19. Cao L, Chen S, Wei M, Guo Q, Liang J, Liu C, Wang M (2019) Effect of laser energy density on defects behavior of direct laser depositing 24CrNiMo alloy steel. Opt Laser Technol 111:541–553. https://doi.org/j.optlastec.2018.10.025
20. JCGM 100: (2008) Evaluation of measurement data - Guide to the expression of uncertainty in measurement (GUM), Bureau International des Poids et Mesures (BIPM), Sèvres (FRA), 2008
21. ISO 4490:2018 (2018) Metallic powders - Determination of flow rate by means of a calibrated funnel (Hall flowmeter). Geneva (CH). International Organization for Standardization (ISO)
22. ISO 3953:2011 (2011) Metallic powders - Determination of tap density, International Organization for Standardization (ISO), Geneva (CH)
23. Saboori A, Piscopo G, Lai M, Salmi A, Biamino S (2020) An investigation on the effect of deposition pattern on the microstructure, mechanical properties and residual stress of 316L produced by directed energy deposition. Mater Sci Eng A 780:139179. https://doi.org/10.1016/j.msea.2020.139179
24. Minitab LLC (2023) Understanding covariates. https://support.minitab.com/en-us/minitab/20/help-and-how-to/statistical-modeling/anova/supporting-topics/anova-models/understanding-covariates/. Accessed 23 October 2025
25. Salmi A, Piscopo G, Pilagatti AN, Atzeni E (2024) Evaluation of porosity in AISI 316L samples processed by laser powder directed energy deposition. J Manuf Mater Process. https://doi.org/10.3390/jmmp8040129
26. Pilagatti AN, Atzeni E, Iuliano L, Salmi A (2023) The role of the carrier gas flow in the directed enegy deposition process. 10th ECCOMAS Thematic Conf on Smart Struct Mater 1258–1269. https://doi.org/10.7712/150123.9873.444102
27. ASTM E384-22 (2022) Standard test method for microindentation hardness of materials, american society for testing and materials (ASTM) international, West Conshohocken (USA)
28. Abdali A, Hossein Nedjad S, Hamed Zargari H, Saboori A, Yildiz M (2024) Predictive tools for the cooling rate-dependent microstructure evolution of AISI 316L stainless steel in additive manufacturing. J Mater Res Technol 29:5530–5538. https://doi.org/10.1016/j.jmrt.2024.03.008
29. Li Y, Bushby AJ, Dunstan DJ (2016) The hall–petch effect as a manifestation of the general size effect. Proc R Soc Lond A Math Phys Eng Sci 472:20150890
30. Bosch Sensortec GmbH (2022) Humidity sensor BME280. https://www.bosch-sensortec.com/products/environmental-sensors/humidity-sensors-bme280/. Accessed 23 October 2025
31. Cengel YA, Ghajar A (2011) Heat and mass transfer (a practical approach, SI version), 2nd edn. McGraw-Hill Education, New York
32. Feynman RP, Leighton RB, Sands M (1965) The feynman lectures on physics; Vol. I. Am J Phys 33:750–752. https://doi.org/10.1119/1.1972241
33. de Nevers N (2012) Physical and chemical equilibrium for chemical engineers, 2nd edn. John Wiley & Sons, Inc., Hoboken, New Jersey
34. Ellis CA, Parbery SA (2005) Is smarter better? A comparison of adaptive, and simple moving average trading strategies. Res Int Bus Finance 19:399–411. https://doi.org/10.1016/j.ribaf.2004.12.009
35. Johnston FR, Boyland JE, Meadows M, Shale E (1999) Some properties of a simple moving average when applied to forecasting a time series. J Oper Res Soc 50:1267–1271. https://doi.org/10.1057/palgrave.jors.2600823

Publisher's note Springer Nature remains neutral with regard to jurisdictional claims in published maps and institutional affiliations.